SATIF-15:
15th Workshop on Shielding aspects of Accelerators, Targets, and Irradiation Facilities

Facility for Rare Isotope Beams (FRIB) at Michigan State University,
East Lansing, Michigan USA
20-23 September 2022.

Session 1: Facility Reports / Shielding & Dosimetry

Table of contents

1. Radiation Transport Simulations in Support of FRIB Initial Operation

Thomas Ginter[1*], Georg Bollen[1], Dali Georgobiani[2], Juan Carlos Zamora[1]
[1]Facility for Rare Isotope Beams, Michigan State University, East Lansing, MI, USA
[2]Fermi National Accelerator Laboratory, Batavia, IL, USA
[*]ginter@frib.msu.edu

The Facility for Rare Isotope Beams (FRIB) at Michigan State University in East Lansing, Michigan, USA has transitioned from being a construction project to user operations for nuclear science experiments. FRIB is designed for the production of rare-isotope beams from in-flight fragmentation and fission of primary beams of stable isotopes ranging from oxygen to uranium with energies up to 200 MeV/u and a beam power of up to 400 kW. This report gives an overview of the radiation transport work carried out to meet the unique challenges of a transitioning facility: support for commissioning and experiment work with beams during final construction; incremental hazard evaluation during beam-power ramp-up; and planning input for staging hazard mitigation strategies.

1.1. Introduction

The Facility for Rare Isotope Beams (FRIB) employs beams of stable isotopes ranging from oxygen to uranium with energies up to 200 MeV/u to produce rare-isotope beams via in-flight fragmentation and fission (Castelvecchi, 2022). The facility started user operations in 2022 with a beam power of 1 kW and is staging for ramp up to full-power operation at 400 kW over the next several years. After an introduction to different radiological areas within the facility, this report describes some recent radiation transport simulations within these environments to support the facility's transition from construction to operation.

1.2. Facility components

In terms of shielding and radiological management, FRIB has several distinct realms. This work will focus on three of these regions: the tunnel, the target hall, and the fast beam area.

Figure 1.1 shows the layout of these areas within the facility. The tunnel, with 6 meters of concrete and earth as shielding separating it from ground level, contains a superconducting radiofrequency linear accelerator (linac). Downstream from the tunnel, the target hall houses the rare-isotope production target, the beam dump, and the first part of the fragment separator. Following the target hall is the fast beam area that houses the rest of the fragment separator as well as locations for performing experiments directly with the fast rare isotope beams. Located downstream from the fast beam area are the stopped and reaccelerated beam areas, where experiments can be performed at lower beam energies.

The tunnel is where the linear accelerator imparts energy and power to the primary beam. Radiation sources from beam interaction with matter are due to typical beam losses along the linac, beam interaction with the charge stripper and charge selector slits, and use of low-power beam dumps for tuning. With the exception of beam fault scenarios, radiation levels are typically low or are mitigated by local shielding.

Figure 1.1. FRIB Layout

Locations for three of the distinct radiological environments discussed in this report: the tunnel, the target hall, and the fast beam area.

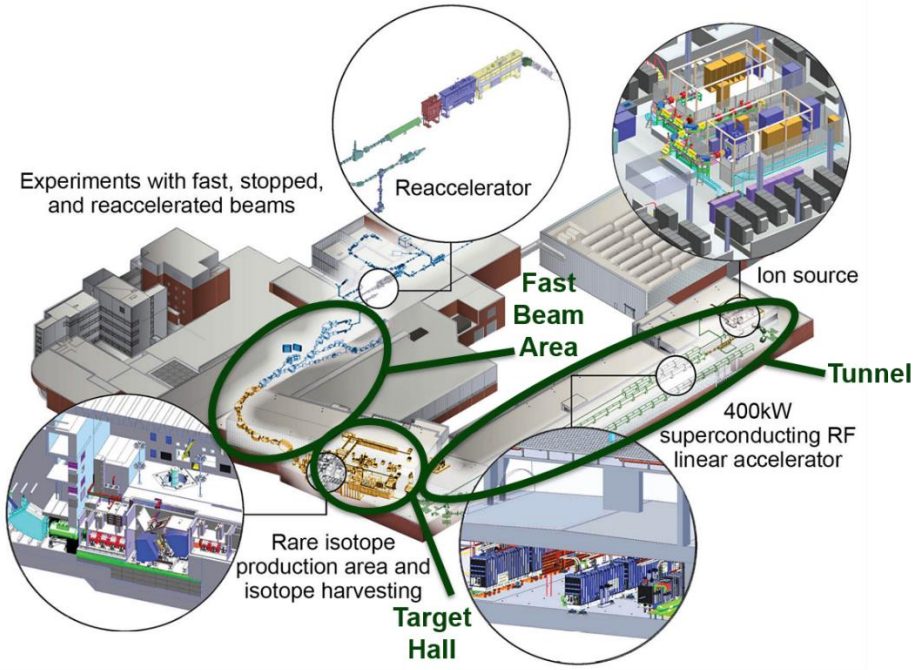

The target hall is the dominant site for the production of radiation within the facility. The primary beam from the accelerator impinges on a production target, depositing up to about 25% of the beam power, to generate the rare isotopes. Unreacted primary beam passing through the target is intercepted with a beam dump. This is where most of the remaining beam power is deposited.

In order to control radiation from the target and the beam dump, the first section of the preseparator is heavily shielded together with the target hall itself. Most beam interactions with matter occur well below ground level. Remote handling capabilities inside the target hall enable replacement of preseparator components. Figure 1.2 shows the fragment separator as it extends from the target hall into the fast beam area.

The fast beam area contains the remaining sections of the fragment separator that transport, further purify, and condition the desired rare-isotope-beams-of-interest to users downstream. It includes a number of shielded vaults where experiments can be conducted with the fast beams. It also contains vaults for beam stopping to convert the fast beams into low-energy beams and for reacceleration.

Almost all of the initial facility beam power has been eliminated from any beams reaching the fast beam area. While the rare isotope beams may maintain an energy close to that of the primary beam, the beam rate is low – typically $<10^9$ particles/s. Prompt and residual radiation is generated when this beam interacts with stops, diagnostic devices, and detectors.

Figure 1.2. FRIB fragment separator extending from target hall into fast beam area

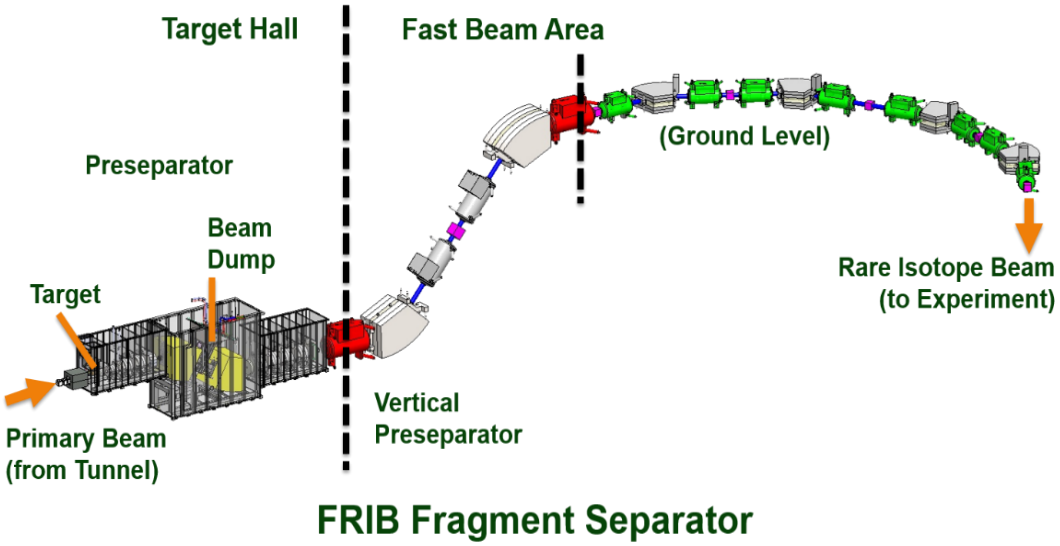

1.3. Examples of radiation transport calculations to support commissioning and start of user operations

FRIB's path from construction to initial operation – and eventually to full power – has required dedicated radiation transport calculations. The radiation transport work conducted to support the design of the facility focused on full power operation – see work presented previously at SATIF (Kostin, 2015, 2021; Georgobiani, 2021a, 2021b). Commissioning and user operation, however, started at low beam power of 1 kW or less. Based on the radiation transport work for full power, the facility design incorporates all necessary shielding components – either as integral parts of the building structure or in the form of space and structural capacity for additions as needed at critical locations. The few-year path to full beam power at 400 kW allows for staging of shielding, infrastructure, and tools during the power ramp up. Hands-on work on target hall components or work on them with local shielding is initially still possible. The transition to full power operation requires the analyses of radiation environments for many different scenarios.

This report will present four examples of such work:

- Radiation calculations to support linac commissioning with beam and to assess required target hall shielding configuration.
- A study of prompt dose rates from beam in the target hall with partial shielding in place.
- Studies of prompt dose rates from beam delivered into the fast beam area.
- An analysis of the target module activation.

The radiation transport code PHITS (Sato et al., 2018) is the tool-of-choice for this work.

1.3.1. Linac commissioning with beam and evaluation of the required target hall shielding configuration

During FRIB construction, it was important to continue installation progress in the target hall at the same time as beam was used in the tunnel for commissioning of the linear accelerator. During the earlier part of final commissioning, some of the shielding in the target hall near the tunnel was not available, and the magnets nearest the tunnel that would normally help provide shielding were not yet installed.

Figure 1.3 provides the estimated dose equivalent rate map along the beam path as calculated for the target hall under this condition. The map results from a two-step calculation. In the first step, neutrons were harvested in the tunnel near the beam entrance to the target hall from the worst case of a 257 MeV/u ^{86}Kr beam at 135 W that was stopped at a nearby beam dump. These neutrons served as the source in the second step of the calculation used to generate the dose rate map presented. This calculation shows that radiation levels remained below 0.1 mrem/h[1] (1 µSv/h) immediately outside of the open target hall roof, even with the shielding roof beams removed. This result meant that the target hall roof beams could be left uninstalled during tunnel beam commissioning to facilitate subsequent target hall installation work.

Figure 1.3. Estimated prompt dose equivalent rates in target hall (elevation view) based on shielding configuration during early portion of final beam commissioning in the tunnel

135 W of 257 MeV/u ^{86}Kr beam delivered to a beam dump in the tunnel near the target hall

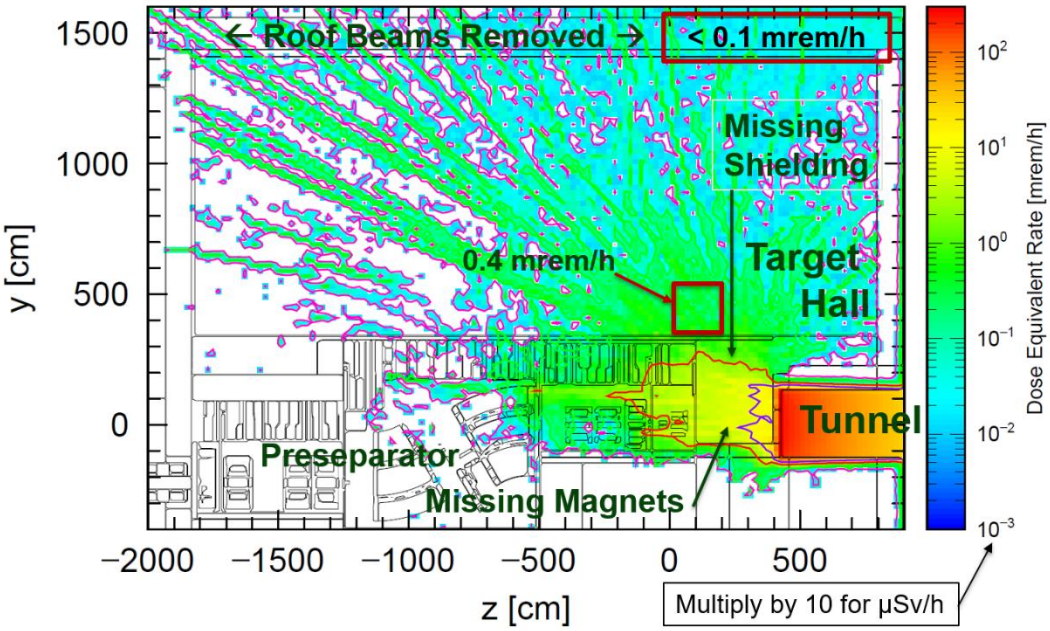

During commissioning of the last segment of the linear accelerator – the part with the highest beam energy and closest to the target hall – the beam delivery magnets in the channel to the target hall were installed. However, the final configuration of shielding in

[1] Since the regulatory limits governing FRIB are based in units of mrem/h, the plots presented in this report are formulated in these units rather than µSv/h.

the target hall above these magnets was not yet available, and temporary shielding was installed. The dose rate map along the beam path given in Figure 1.4, calculated for this scenario using the same beam and technique as just described, shows that radiation levels remain low enough at accessible areas inside the target hall to allow the presence of workers. This result meant that installation work could continue inside the target hall during linac commissioning in the tunnel.

Figure 1.4. Estimated prompt dose equivalent rates in target hall (elevation view) based on shielding configuration during last portion of final beam commissioning in the tunnel

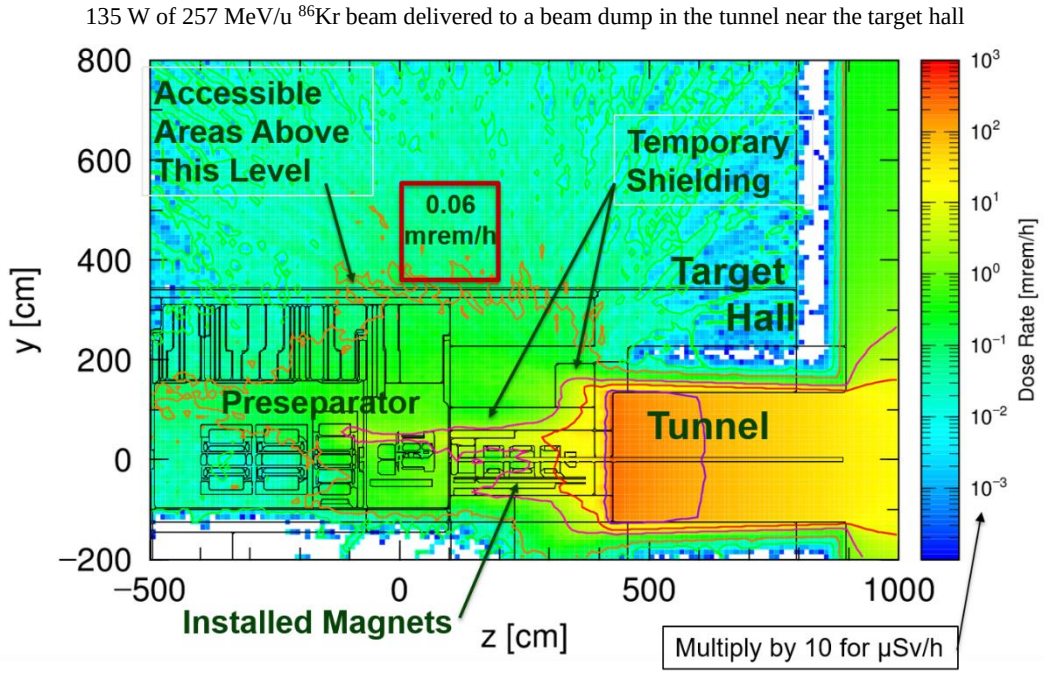

1.3.2. Studies of prompt dose rates from beam in the target hall with partial shielding in place

FRIB had to demonstrate one of its major milestones, identification of its first rare-isotope beam, prior to the completion of installation work in the fast beam area. This work took place in the target hall using detectors and a beam stop installed at the end of the preseparator section inside the target hall. The dose equivalent rate map along the beam path given in Figure 1.5 results from the worst-case of a 1-W beam of 257 MeV/u ^{86}Kr reaching the final beam stop, although a much smaller beam intensity was used for the test. Limits to the maximum beam power delivered into the target hall (or beyond, to the fast beam area) are ensured by a comprehensive set of machine operation modes combined with redundant hardware-based controls. Figure 1.5 shows that with access restrictions, work in the fast beam area could carry on and the roof beams on top of the shielded ground-level beam channel could be left open to facilitate subsequent installation work.

Figure 1.5. Estimated prompt dose equivalent rates from beam commissioning in target hall (elevation view)

1 W of 257 MeV/u ^{86}Kr beam stopping near the exit of the target hall

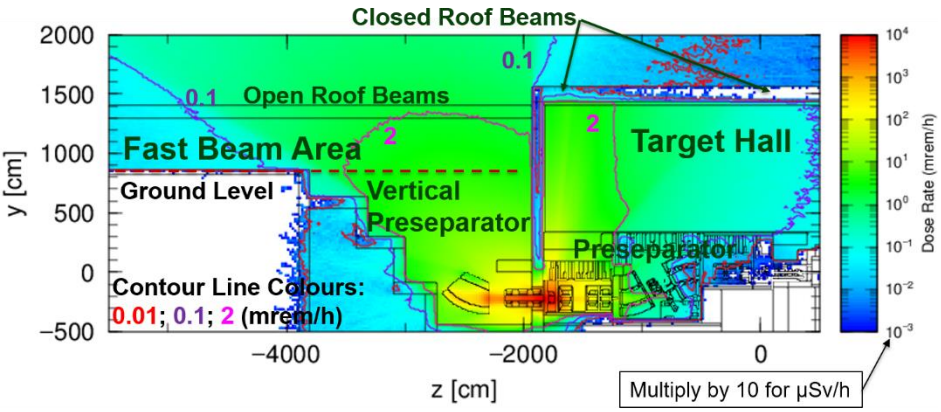

1.3.3. Studies of prompt dose rates from beam delivered into the newly reconfigured fast beam area

FRIB needed to complete its final milestone – delivery of beam to the end of the fragment separator – while roof beams were left open to support subsequent experiment setup and downstream construction. Another important facility priority was to enable users to conduct first experiments as early as possible. The first experiment was set up in the same part of the fast beam area shielding that houses the downstream end of the fragment separator.

The dose equivalent rate map given in Figure 1.6 is calculated with the worst-case beam of 257 MeV/u ^{36}Ar stopping at the end of the fragment separator. It was calculated assuming a beam power of 1 W. It shows that beam delivery is possible if access to neighbouring areas is controlled and the beam power is limited to 0.2 W.

Figure 1.6. Estimated prompt dose equivalent rates in fast beam area (plan view) for beam delivered to the end of the fragment separator with open roof beams for final commissioning work

257 MeV/u ^{36}Ar at 1 W stopping at the exit of the fragment separator

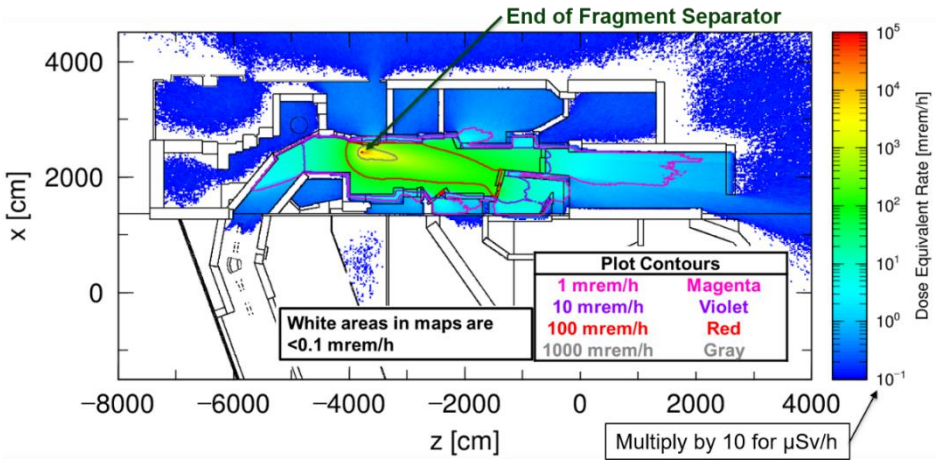

Figure 1.7 gives the dose equivalent rate maps calculated for a typical beam of 160 MeV/u ^{48}Ca stopping with a power of 1 W at the temporary experiment location with roof beams in place over the fast beam area containing the device. It shows that there is no problem with access to neighbouring sections of the fast beam area even if their roof beams remain open for a beam-power limit of 0.2 W.

Figure 1.7. Estimated prompt dose equivalent rates in fast beam area (plan view) for beam delivered to the temporary location of the FRIB Decay Station with roof beams installed for first FRIB experiments

160 MeV/u ^{48}Ca at 1 W stopping at temporary location of the FRIB Decay Station

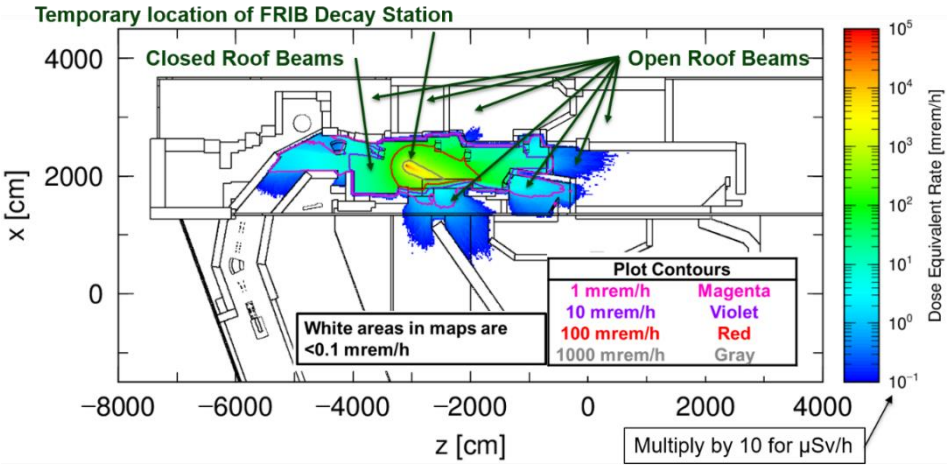

Figure 1.8 gives the dose equivalent rate maps calculated for a typical beam of 160 MeV/u ^{48}Ca stopping with a power of 1 W in one of the new experimental vaults. The calculation was done with no roof beams in place on the new vault since the setup there will be deployed with a much lower beam intensity.

Figure 1.8. Estimated prompt dose equivalent rates in fast beam area (plan view) for beam delivered to the future location of the FRIB Decay Station

160 MeV/u ^{48}Ca at 1 W stopping in one of the experimental vaults

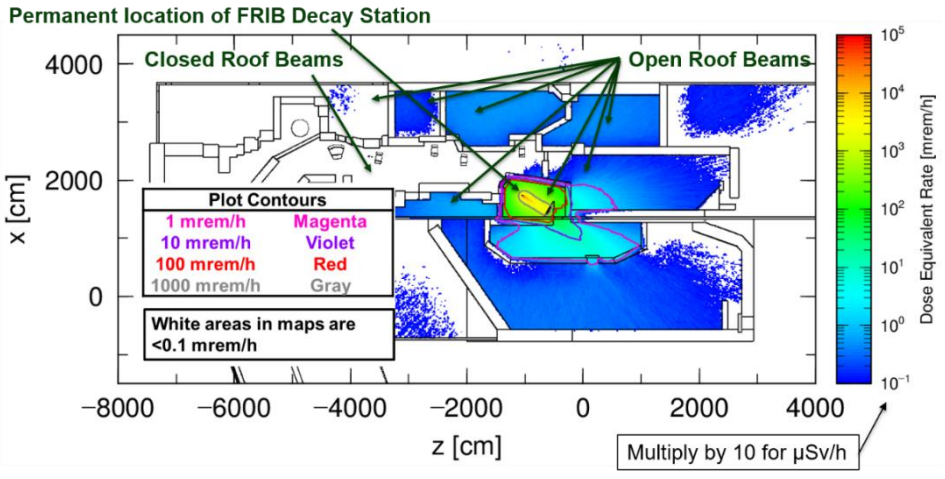

1.3.4. Target module activation analysis

The target module located at the front of the preseparator provides a water-cooled mounting point for the rare-isotope production target. It has the capability to rotate the target to extend its life by distributing beam power and radiation damage over a larger area. The module can be removed from the preseparator remotely by crane to allow for regular replacement of the target as needed either in response to beam damage or to optimize the target thickness for different rare-isotope beams.

Given that hands-on work with the system is still possible for initial low-power operations, analysis of activation of the target and of the target module components provides crucial input for planning system maintenance and staging the remote handling capabilities for target replacement.

Figure 1.9 provides views of the target assembly from the radiation transport model at various stages of disassembly to reveal some of the components included in the simulations. It shows how these parts are subdivided into sections closer to or farther away from the beam interaction point to yield more realistic estimates.

Figure 1.9. Views from the radiation transport model of the FRIB target module at various stages of disassembly

Parts near the beam are subdivided to give more accurate simulation results.

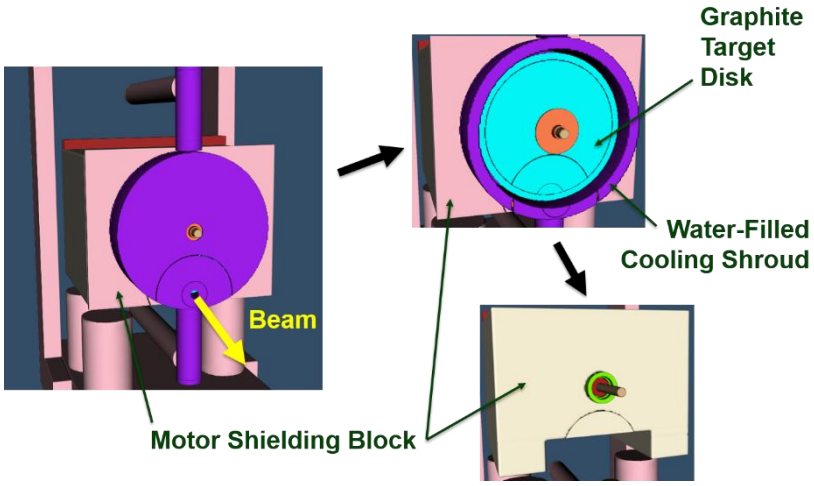

For this work two configurations of the target system were analysed: one was a fixed beryllium target for use with beams below 1 kW, the other a rotating graphite target disk for use with beams with higher power. Figure 1.10 shows the residual gamma-ray flux maps after a cooling time of 1 day calculated from a typical beam of 173 MeV/u ^{48}Ca at 1 kW impinging for 1 week either on an 8.9-mm-thick beryllium target block or on a 10 mm-thick graphite disk. Figure 1.11 shows the estimated residual dose equivalent rate maps from gamma rays calculated at a distance of 30 cm from the module surface after exposure of the rotating graphite target configuration to the beam continuously for 1 week after a cooling time of 1 day.

Figure 1.10. Estimated residual gamma-ray flux calculated for two versions of the FRIB target module (elevation views)

1 kW ^{48}Ca @ 173 Mev/u: 1-week exposure, 1-day cooling. Flux planes pass through beam interaction point.

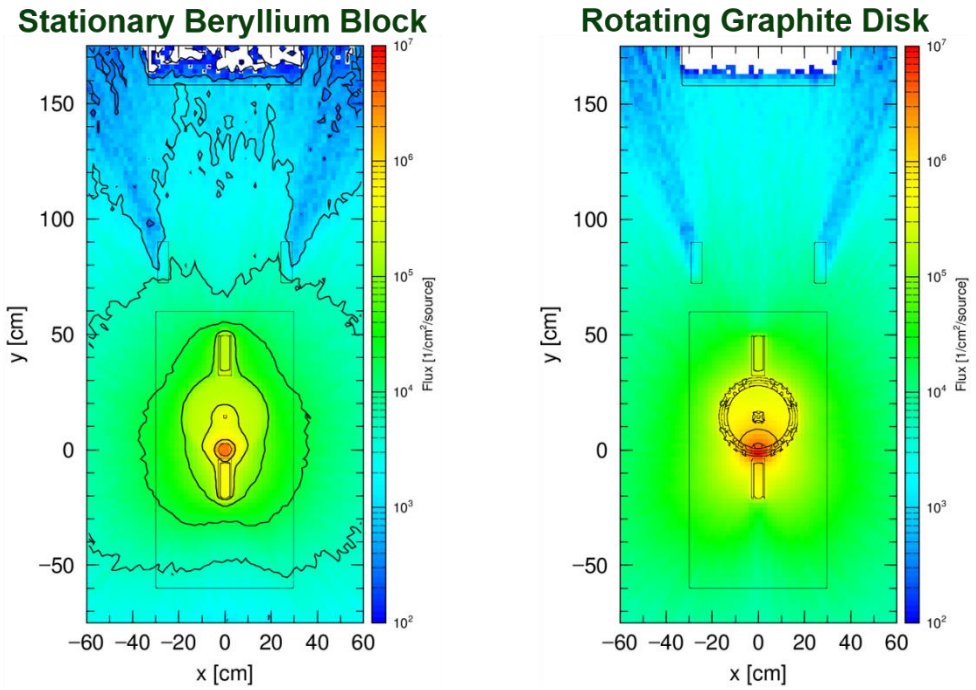

1.4. Summary and conclusions

FRIB is an important new national user facility to produce and study rare isotopes. It has a suite of distinct radiological environments. These include: the tunnel containing the accelerator for the primary beam, the target hall for producing rare isotopes, and the fast beam area for refining and using the rare-isotope beams. These environments and radiation levels are evolving as the facility's beam power increases. Four examples of radiation transport work to support this transition have been presented: an analysis of shielding for target hall installation work in the context of beam commissioning in the tunnel; prompt dose rates from beam in the target hall; prompt dose rates from beam in the fast beam area; and an analysis of the target module activation at low beam power.

This material is based upon work supported by the U.S. Department of Energy, Office of Science, Office of Nuclear Physics and used resources of the Facility for Rare Isotope Beams (FRIB), which is a DOE Office of Science User Facility, under Award Number DE-SC0000661.

Figure 1.11. Estimated residual dose equivalent rates calculated at a distance of 30 cm from the FRIB target module with the rotating graphite target disk (elevation views)

1 kW ^{48}Ca @ 173 Mev/u: 1 week exposure, 1 day cooling

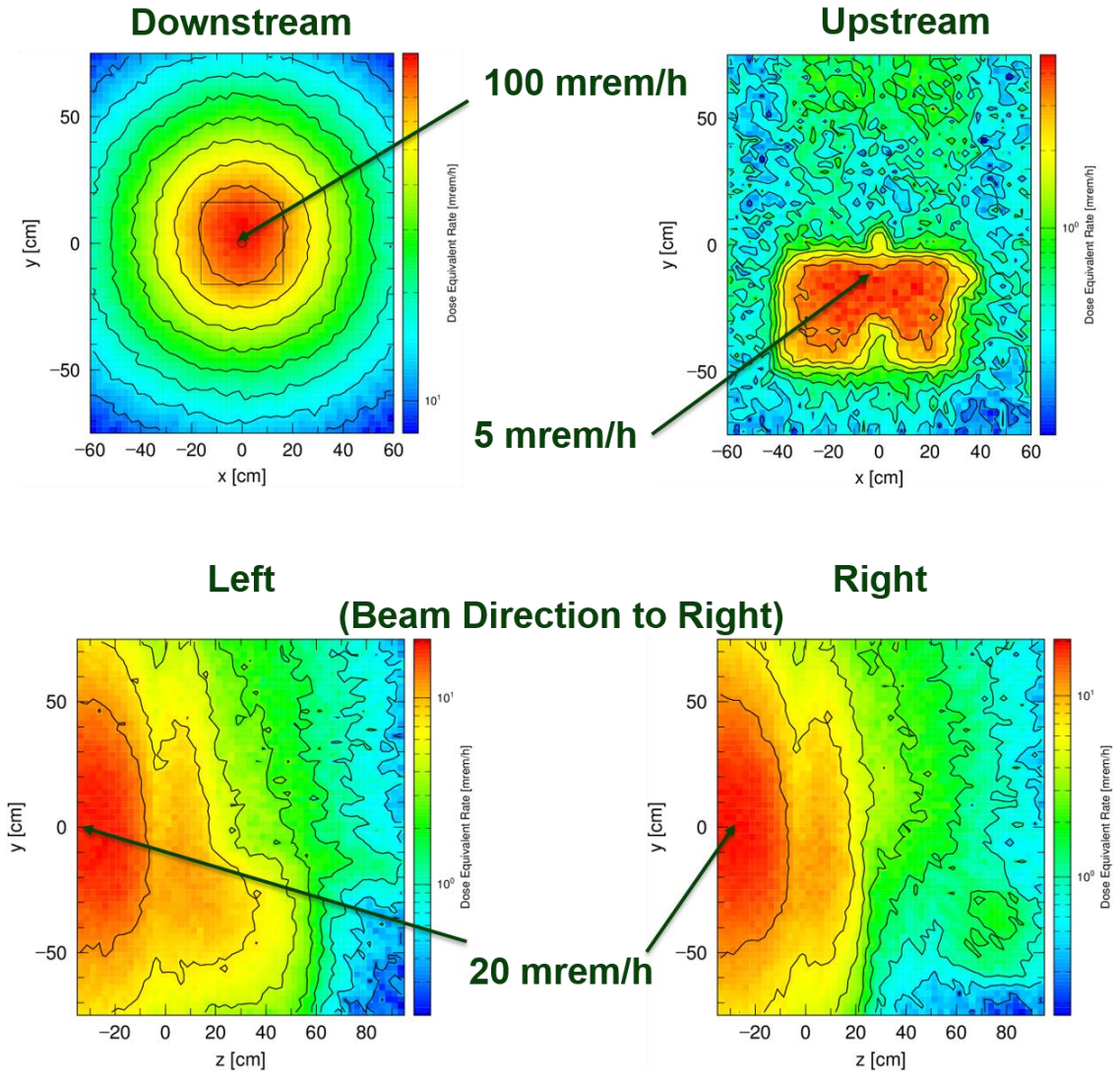

1.5. List of references

D. Castelvecchi, "Long-awaited accelerator ready to explore origins of elements", Nature 605, 201-203 (2022), https://doi.org/10.1038/d41586-022-00711-5.

D. Georgobiani, G. Bollen, E. Burkhardt, M. Hausmann, M. Portillo (2021a), "Radiation Heat Load and Coil Lifetime Calculations in Support of FRIB Magnet Design", NEA (2021), Shielding Aspects of Accelerators, Target and Irradiation Facilities (SATIF-13) - Proceedings of the Thirteenth Meeting, 10-12 October 2016, Dresden, Germany, OECD Publishing, Paris.

D. Georgobiani, M. Kostin, G. Bollen (2021b), “Radiation environment studies for the Facility for Rare Isotope Beams at MSU”, NEA (2021), Shielding Aspects of Accelerators, Targets and Irradiation Facilities (SATIF-14), OECD Publishing, Paris

M. Kostin, R. Lowrie, R. Ronningen (2015), “Evaluation of radiation environment at FRIB linac”, NEA (2015), Shielding Aspects of Accelerators, Target and Irradiation Facilities (SATIF-12), OECD Publishing, Paris.

M. Kostin, B. Blunt, D. Georgobiani, R. Lowrie, J. Northum, and R. Ronningen (2021), “Annual Doses to Personnel and General Public from Direct Exposure, Skyshine and Airborne Emissions at FRIB”, NEA (2021), Shielding Aspects of Accelerators, Target and Irradiation Facilities (SATIF-13) - Proceedings of the Thirteenth Meeting, 10-12 October 2016, Dresden, Germany, OECD Publishing, Paris.

T. Sato, Y. Iwamoto, S. Hashimoto, T. Ogawa, T. Furuta, S.-I. Abe, T. Kai, P.-E. Tsai, H. N. Ratliff, N. Matsuda, H. Iwase, N. Shigyo, L. Sihver and K. Niita (2018), “Features of Particle and Heavy Ion Transport code System (PHITS) version 3.02”, J. Nucl. Sci. Technol. 55, 684, 2018.

1.6. List of abbreviations and acronyms

FRIB	Facility for Rare Isotope Beams

2. Overview of Shielding Analyses at Oak Ridge National Laboratory's Spallation Neutron Source Second Target Station

Thomas M. Miller*, Kristel Ghoos, Ahmad Ibrahim, Tucker McClanahan, Kumar Mohindroo, Paul Mueller, Igor Remec, Wouter de Wet, and Lukas Zavorka
Oak Ridge National Laboratory, Spallation Neutron Source, Second Target Station Project, Oak Ridge, Tennessee, USA
*millertm@ornl.gov

The Neutronics Group for the Second Target Station project at Oak Ridge National Laboratory is responsible for all neutronics analyses related to the design and construction of the Second Target Station. This paper provides an overview of four analyses that are representative of all the ongoing neutronics work for the project but especially highlights tasks related to shielding. These analyses extend from the proton accelerator through the target monolith and bunker to the end of a neutron beamline. Each example highlights the tools and methods that the Neutronics Group uses for analysis. The primary tool is the Monte Carlo radiation transport code MCNP6, augmented by auxiliary codes that supplement the input preparation and the output processing. The supporting codes specifically highlighted in this paper are Attila4MC, ADVANTG and AARE.

2.1. Introduction

The design of the Second Target Station (STS) at Oak Ridge National Laboratory's (ORNL's) Spallation Neutron Source (SNS) is currently underway (STS, 2020). STS will operate at 700 kW of 1.3 GeV protons with short pulses less than 1 μs and a repetition rate of 15 Hz. The new target will be a rotating, water-cooled tungsten target, which will have two coupled cryogenic moderators—one above the target and the other below—filled with liquid parahydrogen. The moderators will be world leaders in cold neutron peak brightness. Sixteen neutron beamlines will view the moderator above the target, and six neutron beamlines will view the moderator below the target. In total, STS will have 22 new instruments.

The STS Neutronics Group is responsible for all neutronics analyses required for the design and construction of STS, which include neutronics optimization of the target and moderator, heating and radiation damage of major components, and all aspects of STS shielding. This paper presents examples of shielding analyses performed for the design of STS. These analyses include shielding along the proton beam tube from the existing accelerator to the second target, activation of the target, shielding cask design of the activated target, energy deposition and radiation damage of the proton beam window (PBW), and shielding along the Chopper Spectrometer Examining Small Samples (CHESS) neutron beamline (Sala et al., 2022) from the target monolith through the bunker and to the instrument 30 metres from the moderator.

The primary computational tool used by the STS Neutronics Group is MCNP6 (Werner, 2017). However, most of these analyses benefit from auxiliary codes that develop input for or process the output from MCNP6. The examples in this paper will highlight the cutting-edge computational methods the STS Neutronics Group uses, such as unstructured mesh geometries converted from computer-aided design (CAD) (Zavorka and Remec, 2021), activation simulations for charged and neutral particles in any energy regime (Gallmeier and Wohlmuther, 2015; Gallmeier and Wohlmuther, 2018; Popova, 2018), and advanced automated variance reduction techniques for beamline shielding with long streaming gaps (Miller, DiJulio, and Santoro, 2020; Mosher et al., 2015).

2.2. Accelerator Magnet Shielding Analysis

A preliminary design phase analysis has been performed to evaluate the need for radiation-hardened magnets at the STS. The protons that strike the tungsten target create high-energy neutrons and other particles, and a fraction of these spallation neutrons and their secondaries will travel back into the accelerator tunnel and the quadrupole magnets therein. Radiation damage degrades the Kapton material, which is the insulating lining within the magnet coil windings. This degradation forms short circuits that, over time, reduce the effectiveness of the magnets. The Kapton in the magnet coil windings is expected to be the limiting component of the magnet, and the threshold dose at which the Kapton lining is expected to fail is 1×10^6 Gy (Ludewig, 2001).

MCNP6.2 was used to model the STS accelerator tunnel and target building interface geometry, as well as to determine the backscatter dose rates in the Kapton components of the final set of quadrupole magnets when the beam is active. A constructive solid geometry (CSG) was used in this analysis that included the accelerator tunnel terminus, where the quadrupole magnet and interface shielding are located; the proton beam tube; and the target building. These components are illustrated in Figure 2.1 and Figure 2.2. In addition to the target, the PBW was another major component within the target building included in this model that affected the analysis.

The accelerator magnet shielding analysis considers two variations with modest changes to the proton beam tube interface shielding geometry. The location and orientation of the magnets in the accelerator tunnel are identical in both cases. The first iteration, or *standard* shield, includes a rectangular block of stainless steel that caps off the otherwise exposed opening of the proton beam outer tube. This stainless steel block is 30 cm thick × 90 cm tall × 90 cm wide. The shielding block is penetrated at the centre by the 27.3 cm diameter proton beam inner tube (see Figure 2.1). The second iteration, or *prototype* shield, moves the beam diameter transition into a set of stacked, cylindrical, stainless steel shields and includes a set of shielding plug sheaths that are placed into the proton beam tube (see Figure 2.2).

The radiation transport models developed for this analysis represent the magnet coil windings as a homogenous mixture of copper and water. Because the failure mechanism is related to the dose in Kapton, the maximum dose used to evaluate the expected lifetime for the nonhardened magnets must reflect energy deposition in Kapton. Without the presence of Kapton in the model, it is not possible to directly tally energy deposition in the Kapton material alone. Instead, kerma factors are applied to photon and neutron cell-averaged flux tallies within the coil windings to estimate the dose in the Kapton components.

In this model, the complex geometry and the large distance between the magnet coils and the target assembly mean that tally convergence using only semianalogue Monte Carlo transport (implicit capture only) would take an unreasonable amount of time. Therefore, DXTRAN spheres were placed around the magnet assemblies and employed for variance reduction to converge the tallies within a reasonable timeframe. The use of DXTRAN spheres in a neutron backscatter dose rate calculation that relies on nuclear models means that the results will certainly be an overestimate, which, in this case, provides conservative results. This overestimation is because of the assumption that particles scattering to DXTRAN spheres in the nuclear model energy regime are isotropic.

Figure 2.1. A focused elevation view sliced through the centre of the beam geometry with the standard shielding configuration.

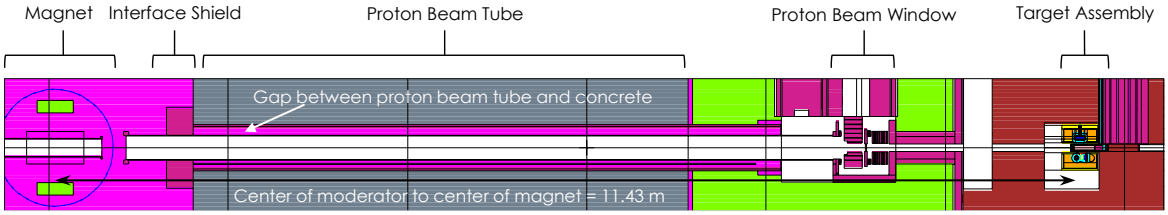

Figure 2.2. A focused elevation view sliced through the centre of the beam geometry with the prototype shielding configuration.

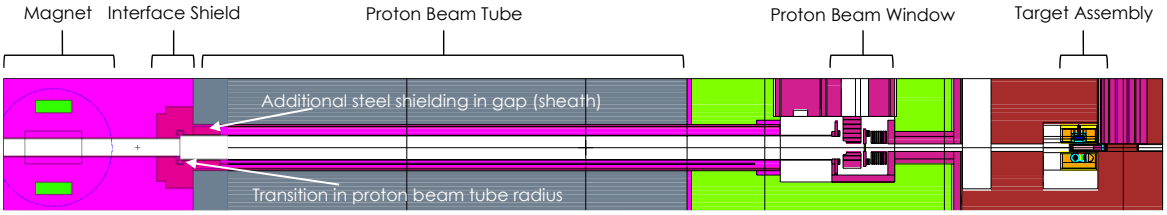

Using the standard interface shielding configuration, the maximum Kapton dose rate in the coil windings was determined to be 6.30 Gy/h ± 1.9%, with the individual neutron and photon components accounting for 4.97 Gy/h and 1.33 Gy/h, respectively. In the case of the prototype interface shielding configuration, the maximum Kapton dose rate in the coil windings was determined to be 2.65 Gy/h ± 5.2%, with the individual neutron and photon components accounting for 2.10 Gy/h and 0.55 Gy/h, respectively. Assuming a duty cycle of 5000 h/year and a threshold failure dose of 1×10^6 Gy, the expected lifetime of the nonhardened quadrupole magnets is 31.7 years for the standard interface shielding configuration and 75.5 years for the prototype interface shielding configuration.

The expected lifetime of nonhardened magnets in the standard configuration suggests that they are unlikely to perform as required for the entirety of the STS facility's planned operational lifetime. However, with relatively simple modifications to the design of the interface shielding, the expected lifetime of nonhardened magnets was increased significantly to greater than 75 years. Therefore, the need for radiation-hardened magnets can be safely avoided if reasonable shielding considerations at the accelerator tunnel–proton beam tube interface are included in the final design.

2.3. Target Segment Activation and Shielding Cask

One of the leading preliminary design candidates for the STS target is a rotating, water-cooled tungsten target with tantalum cladding housed in a stainless steel shroud. The rotating target is divided into 21 independent segments. These target segments will become highly activated because of spallation reactions and nuclei transmutation by primary protons and emitted neutrons. Decay dose rates generated from the target segments, once they are removed from their location within the core vessel, must be quantified to determine the shielding configurations of remote handling tools and transport casks, as well as to aid in planning maintenance activities. This analysis evaluated the activation of a single target segment and the cask shielding requirements. To complete this evaluation, an approach using a hybrid unstructured mesh (UM) geometry and CSG (Zavorka and Remec, 2021) was used to calculate spallation products and neutron fluxes. The UM portion of the geometry was created using the Attila4MC code (Silver Fir Software, 2020) with

SpaceClaim CAD models. The spallation products and neutron fluxes from MCNP6.2 were input to activation calculations with the aare_activation script, which part of the AARE package (Gallmeier and Wohlmuter, 2018) that includes CINDER2008 (Popova, 2018). Then AARE was used to produce the decay photon source at different cooling times. The ADVANTG code was used to accelerate the final decay photon transport calculation (Mosher et al., 2015).

Figure 2.3 shows the geometry of a single target segment after it has been subdivided to represent the spatial dependence of the neutron flux and photon source more accurately throughout the segment. In Figure 2.3, the orange is tungsten, blue is SS316, and dark outline around tungsten is the tantalum cladding. Figure 2.4 shows the tungsten target segment (red) in a notional stainless steel 316 or lead cask, which is represented by the colour blue. The green colour in Figure 2.4 is air.

Figure 2.3. Single target segment.

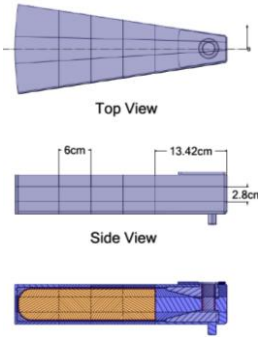

Figure 2.4. Notional cask with target segment.

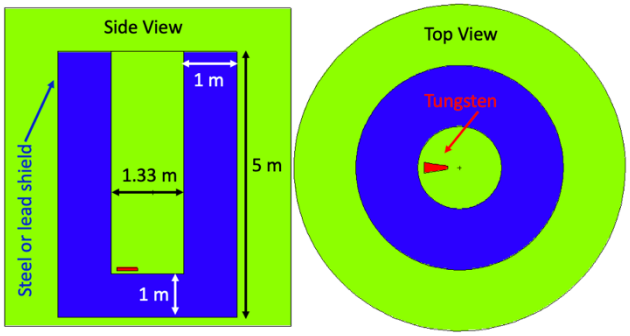

The decay photon transport calculation through the thick stainless steel or lead cask exhibited between 25 and 30 orders of magnitude attenuation depending on the shield material and consequently required advanced variance reduction. ADVANTG does not support the volumetric sources created for the MCNP6.2 UM capability, so an approximate source was created for this problem. This source approximation used on decay photon energy distribution that was the average of the energy distribution in each UM voxel, and it used a flat spatial distribution throughout the volume of the segment. This approximate source was needed to run the ADVANTG calculation to generate the weight windows. It was also essential to develop source biasing parameters that were crucial for dramatically accelerating the decay photon transport in this problem.

Figure 2.5 shows some results of the photon transport simulations with the activated target segment in a steel or lead cask. The operations scenario assumed for this analysis was a 700 kW proton beam on the target for 5000 hours per year for 10 years. Following this operations scenario and 1 additional week of cooling time, if the allowed dose rate on the outside of the cask is 1000 μSv/h (100 mrem/h), then the shield needs 33.8 cm of stainless steel or 20.5 cm of lead. If the target dose rate on the surface of the cask is 50 μSv/h (5 mrem/h), then the shield needs 40 cm of stainless steel or 24.8 cm of lead. If 1 year of cooling time follows the operations scenario, then 29 / 18.9 cm or 35.5 / 23.6 cm of stainless steel / leading are needed for dose rates on the surface of the cask of 1000 μSv/h (100 mrem/h) or 50 μSv/h (5 mrem/h), respectively.

Figure 2.5. Photon effective dose profile through a steel and lead cask after (*left*) 1 week and (*right*) 1 year of cooling time.

The grey shading represents the cask. The centre of the target segment is 2.5 cm above the bottom of the cask.

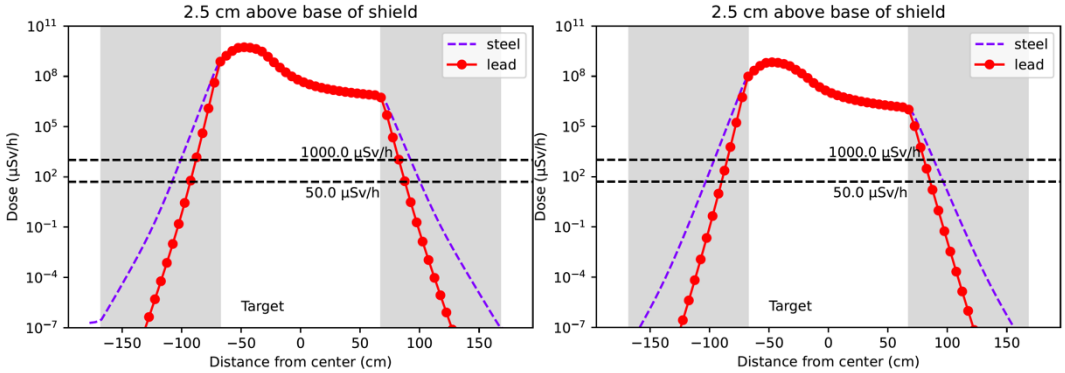

2.4. Proton Beam Window Analysis

The PBW provides a barrier between the high-vacuum accelerator atmosphere and the core vessel atmosphere. This 5 mm thick aluminium window is actively cooled with water. The assembly around the PBW contains a collimator, cooled and uncooled shielding, bellows, a remote clamp, and other items. Above the PBW assembly, more shielding is present. To design the required cooling for the PBW and its assembly, the heating rates must be known. The lifetime of the PBW is determined by the displacements per atom (dpa) and helium concentration material limits. The goal of the proton beam window analysis is to provide detailed information on heating, dpa, and helium production rates in the PBW, the assembly around the PBW, and the shielding above it.

The MCNP6.2 model used a detailed UM geometry, which was generated by Attila4MC based on a SpaceClaim model of the PBW design. To facilitate the meshing, the SpaceClaim model was simplified by removing unnecessary details such as chamfers and rounded corners. Additionally, the small round water channels (3 mm diameter) that cool the PBW were replaced by square water channels with the same volume. This shape allows for coarser meshing without significantly changing the total water volume. The UM for the PBW assembly and the shielding above the assembly was inserted into a CSG model of the target monolith, which included the target, moderators, shielding blocks, and other items. Therefore, the resulting model was a hybrid UM/CSG geometry. For this analysis, an octupole proton beam profile was used, with a beam footprint on the target of approximately 90 cm^2. No variance reduction was used, and sufficiently large mesh element sizes were chosen to obtain good statistics (<10% relative error) in the important regions of the geometry after a reasonable simulation time.

An important benefit of the UM is the capability to tally quantities on a mesh that accurately represents complex geometry features. This ability is a huge improvement to a structured mesh such as the orthogonal FMESH and TMESH options in MCNP, in which several materials can be included in one mesh cell. The UM data can be directly used for further engineering analysis of each component. In this analysis, detailed heating rate distributions tallied on UM mesh and average heating per component (with +F6 tallies) were calculated. To calculate the dpa, the neutron and proton fluxes were scaled by flux-to-dpa conversion factors (Lu, Wechsler, and Dai, 2006; Lu et al., 2006; Lu and Wechsler, 2007; Lu et al., 2012).

When protons interact with the material (as is the case for the PBW and the components close to and downstream of the PBW), most of the energy deposition comes from ionization paths of the protons that are slowing down. In components upstream of and further away from the PBW, photons provide the highest contribution to the energy deposition. The contribution of neutrons is small through the whole PBW assembly. The total (sum of the proton, photon, and neutron) energy deposition distribution in the PBW assembly and the shielding above is shown in Figure 2.6. The maximum energy deposition density of 5.4 J/cm^3 for one pulse occurs in the PBW that directly interacts with the proton beam. The energy deposition through the middle of the PBW (see Figure 2.7) gives a clear impression of the proton beam shape. Further away from the proton beam, the heating rates quickly decrease.

Figure 2.6. Energy deposition in the PBW assembly and shielding in a vertical cut through the geometry along the proton beam direction.

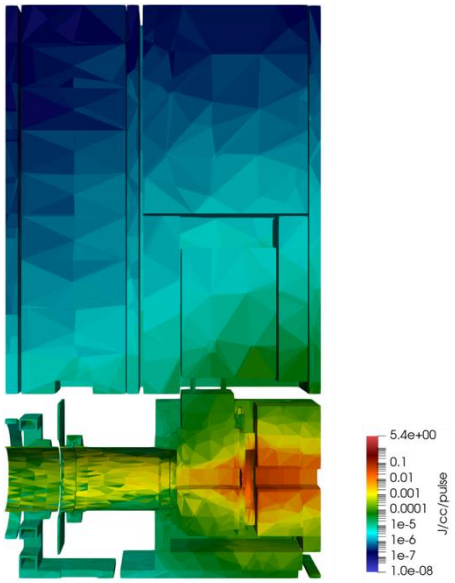

Figure 2.7. Energy deposition in a plane perpendicular to the proton beam direction through the middle of the PBW.

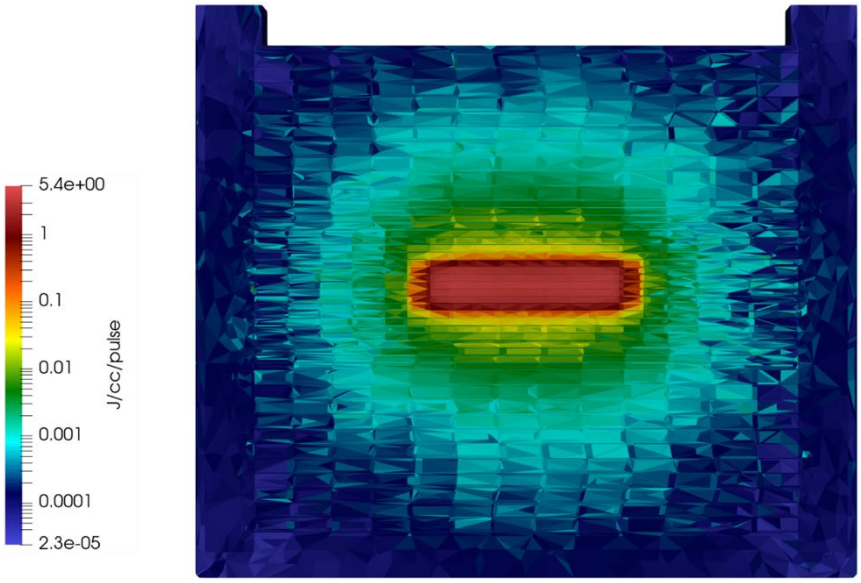

For the aluminium in the PBW, the lifetime limit due to radiation damage is 40 dpa and for helium production is 2000 appm (atomic parts per million). With the calculated maximum of 1.1 dpa/year and 660 appm helium/year, the expected lifetime of the PBW is 36 years based on dpa and 3 years based on helium production. The helium production is the limiting contributor. Comparing these results with earlier results from June 2020 reveals interesting information (see Table 2.1). The earlier results were obtained with a smaller proton beam (62 cm^2), a PBW with 10 mm thickness, a CSG geometry and TMESH tallies. Despite these differences, the maximal values are very similar to those obtained in the current (July 2022) analysis.

Table 2.1. Lifetime prediction of the PBW, based on the calculated maximum dpa and helium production.

	Results June 2020	Results July 2022	Lifetime limit
Maximum He rate	616 appm/year	660 appm/year	2000 appm Resulting lifetime 3 years
Maximum dpa rate	1.07/year	1.1/year	40 dpa Resulting lifetime 36 years

2.5. CHESS Neutron Beamline Shielding

CHESS will be one of the first instruments designed, built, and commissioned at the STS. The neutronics group is responsible for analysing all aspects of CHESS shielding. Completed so far for the CHESS preliminary design are analyses of the shielding along the beamline outside of the bunker, the detector vessel, and the neutron beam stop. A high-level overview of the CHESS geometry is shown in Figure 2.8, which illustrates the location of these components with respect to the target monolith, bunker, and instrument detector. The target monolith (not shown in the figure) extends from the left of Figure 2.8 to the right edge of the monolith insert in Figure 2.8 is the shielding surrounding the rotating target and the moderators. From the right edge of the monolith insert to the right edge of the bunker wall in Figure 2.8 is where the bunker and bunker wall are located.

Figure 2.8. CHESS geometry overview, with a total flight path of 34 m from moderator to detectors.

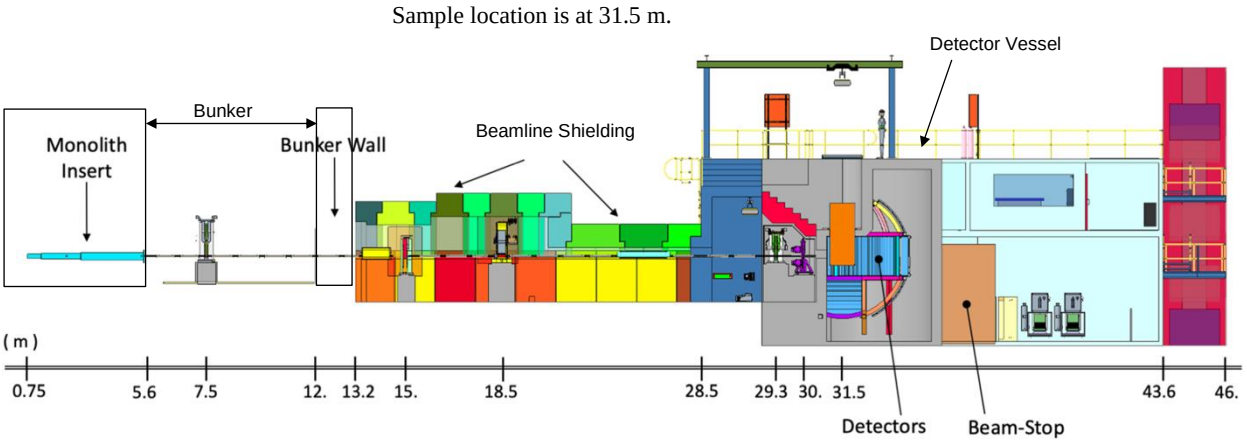

Source: Sala et al., 2022.

Simulations of the CHESS beamline were performed with the ST11 neutron beamline source that was created for preliminary shielding analyses of the STS bunker, beamlines, and instruments (Miller and Remec, 2022). MCNP6.2 was used for the simulations, and a patch that implements neutron supermirror physics was applied to the MCNP6.2 source code (Magán and Bergmann, 2020). The CHESS neutron guide is expected to use an $M = 6$ neutron supermirror and have an octagonal cross-sectional area. The simulations used flux-to-dose conversion factors typically used by SNS and STS, which are based on ICRP Publication 74 (Popova, 2012). ADVANTG was used to generate variance reduction parameters (Mosher, 2015). However, a special Lobatto quadrature set was needed for the deterministic transport simulations in ADVANTG because the neutron beamline itself is a long streaming gap from the moderator to the instrument (Miller, DiJulio, and Santoro, 2020).

Analysis of the CHESS beamline shielding between the bunker and detector vessel shows that the walls and roof need to be around 90 cm of high-density concrete at the bunker wall and decreases to ~50 cm at the detector vessel. These thicknesses are needed to meet the dose rate requirement of 2.5 μSv/h (0.25 mrem/h) for the generally accessible areas on the outer surface of the beamline shielding However, one significant deviation is illustrated in Figure 2.9. This figure shows an elevation view of total dose rate contours along the centre of the CHESS beamline. A white circle in Figure 2.9 highlights a location where the roof of the CHESS beamline shielding needs 140 cm of high-density concrete. This thickness is driven by a transition of the internal height of the beamline shielding and could be reduced if that height was more consistent.

Figure 2.9. Elevation view of total effective dose rate contours (µSv/h) along the CHESS beamline shielding between the bunker wall and detector vessel (dimensions in centimetres).

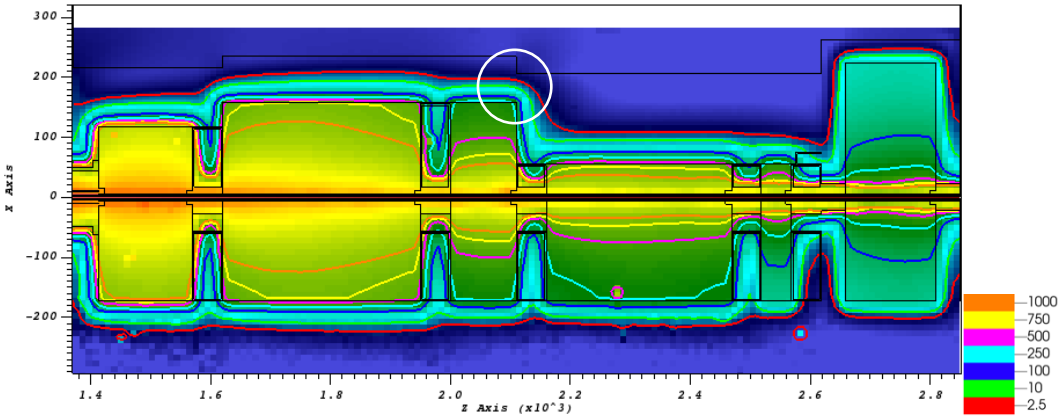

Next, the detector vessel and beam stop were analysed. The goal was to ensure that the dose rate on the outer surface of the detector vessel and beam stop was 2.5 µSv/h (0.25 mrem/h) or less. The detector vessel is 31.5 cm of polyethylene between two 2.5 cm thick layers of stainless steel. The beam stop is made from the high-density concrete, the same material that is used for the beamline shielding, and it extends 120 cm above and to the left and right of the centre of the neutron beam. Below the centre of the neutron beamline, the beam stop extends down to the floor of the room downstream of the detector vessel. Two simulations were performed to complete the CHESS analysis, and both analyses were with the full white beam of the ST11 source. The first simulation did not have a sample intercept the beam in the detector vessel, so the radiation exiting the beamline continued straight ahead to the beam stop. The second simulation had a 1 cm thick stainless steel sample that was large enough to intercept the entire neutron beam. This sample was thick enough that nearly all the low-energy neutrons were absorbed in the sample and converted to capture gamma rays. The dominant captured gamma rays created by iron had energy around 7.6 MeV, which is a significant source considering the detector vessel is mostly polyethylene. Figure 2.10 shows total dose rate contours in the centre of the CHESS detector vessel and beam stop. The left image shows the contours without the sample, and the right shows them with the sample. The results of these simulations show that the detector vessel is adequately thick for both situations. The beam stop needs to extend 275 cm beyond the back of the detector vessel, but this includes a 50 cm long void; so-called *get lost* tube in the beam stop, which is needed to reduce the backscattering of the neutron beam towards the sample location. Without the stainless steel sample, the beam stop design is adequate. With the stainless steel sample, the beam stop needs to be approximately 10 cm taller.

Figure 2.10. Elevation view of total effective dose rate contours (μSv/h) at the centre of the CHESS detector vessel and beam stop.

The left model has no sample, and the right model has a 1 cm thick stainless steel sample (dimensions in centimetres).

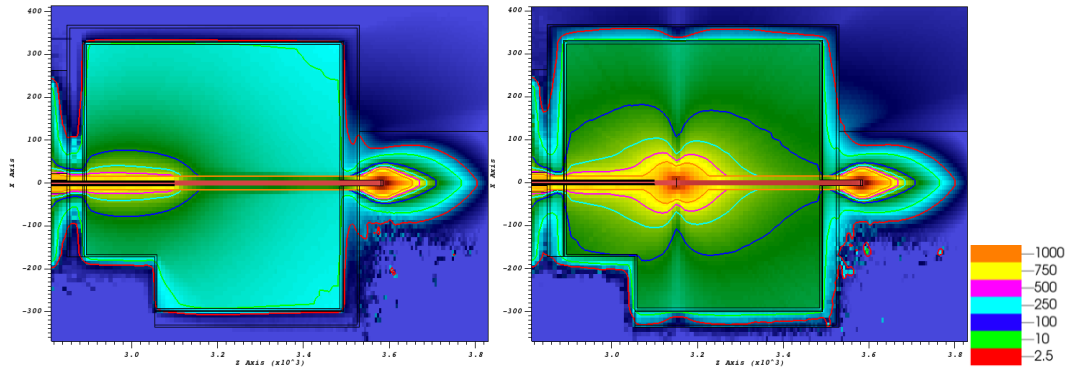

2.6. Summary and Conclusions

These examples of shielding analyses at the STS project illustrate how the STS Neutronics Group is performing many cutting-edge analyses with state-of-the-art radiation transport tools. MCNP6.2 simulations are supplemented by UM geometry and variance reduction parameters from Attila4MC, variance reduction parameters generated by ADVANTG, and activation calculations and generation of decay gamma sources by AARE. The examples described in this paper are limited to shielding applications: protecting components of an accelerator magnet, calculating the activation of a single target segment and the required shielding cask, estimating heating rates in the proton beam window and the window lifetime, and estimating the shielding requirements of the CHESS beamline shielding, detector vessel, and beam stop. However, many other important tasks are performed by the STS Neutronics Group, such as the neutronics optimization of the target and liquid hydrogen moderators (Zavorka et. al., 2022). The goal of the STS Neutronics Group is to work closely with the scientists and engineers designing the STS and its associated instruments so these state-of-the-art radiation transport tools can be used early in the design process to minimize the differences between the engineering design and physics models used in radiation transport. This collaboration will lead to building the world's brightest source of cold neutrons and a facility that will be world-leading for several decades.

2.7. List of references

Gallmeier, F. X. and M. Wohlmuther (2015), "The Residual Nuclei Path of MCNPX 2.6.0 and 2.7.0", TM-85-15-03, Paul Scherrer Institut.

Gallmeier, F. X. and M. Wohlmuther (2018), "AARE_ACTIVATION Script Version 2.0 User Guide", ORNL/TM-2018/1036, Oak Ridge National Laboratory.

Lu, W., M. S. Wechsler, and Y. Dai (2006), "The NCSU Radiation Damage Database; Proton-Induced Damage Energy and Application to Radiation Damage at SINQ", *J. Nucl. Mater.*, **356**, pp. 280–286.

Lu, W. et al. (2006), "Spallation Radiation Damage Calculations and Database: Cross-Section Discrepancies between the Codes", *J. ASTM Inter.*, **3**, 7, pp. 212–219, DOI: 10.1520/JAI13467.

Lu, W. and M. S. Wechsler (2007), "The Radiation Damage Database: Section on Helium Cross Section", *J. Nucl. Mater.*, **361**, pp. 282–288.

Lu, W. et al. (2012), "A Reevaluation of Radiation Damage Cross Sections", *J. Nucl. Mater.*, **431**, pp. 33–38.

Ludewig, H. (2001), "Estimate of Dose on 36Q85 Quadrupoles in RTBT", R105101000-CA000, Oak Ridge National Laboratory.

Magán, M. and R. M. Bergmann (2020), "Supermirror Physics with Event Biasing in MCNP6", *Nucl. Instrum. Methods Phys. Res., Sect. A*, **955**, 163168, DOI: 10.1016/j.nima.2019.163168.

Miller, T. M., D. D. DiJulio, and V. Santoro (2020), "Application of ADVANTG Variance Reduction Parameters with MCNP6 at ESS", *J. Neutron Res.*, **22**, 199, DOI: 10.3233/JNR-200158.

Miller, T. M. and I. Remec (2022), "Second Target Station Project Generation of Beamline Sources–Preliminary Design", ORNL/TM-2022/1828, Oak Ridge National Laboratory, DOI: 10.2172/1871100.

Mosher, S. W., et al. (2015), "ADVANTG—An Automated Variance Reduction Parameter Generator", ORNL/TM-2013/416, Rev. 1, Oak Ridge National Laboratory.

Popova, I. I. (2012), "Flux to Dose Conversion Factors", SNS-NFDD-NSD-TR-0001, R02, Oak Ridge National Laboratory.

Popova, I. I., ed. (2018), "An Updated Manual for CINDER2008 Codes and Data in the AARE Package", ORNL/TM-2018/926, Oak Ridge National Laboratory.

Sala, G., et al. (2022), "CHESS: The future direct geometry spectrometer at the second target station", *Rev. Sci. Instrum.*, **93**, 065109, DOI: 10.1063/5.0089740.

Silver Fir Software, Inc. (2020), "Attila4MC 10.2, Overview of Core Functions", SFSW-UR-2020-OCF102, Silver Fir Software, Gig Harbor, Washington.

STS (2020), "Spallation Neutron Source Second Target Station Conceptual Design Report Volume 1: Overview, Technical and Experiment Systems", S01010000-TR0001, R00, Oak Ridge National Laboratory.

Werner, C. J., ed. (2017), "MCNP User's Manual, Code Version 6.2", LA-UR-17-29981, Los Alamos National Laboratory.

Zavorka, L. and I. Remec (2021), "Neutron dose rate calculation with the MCNP6 hybrid geometry model of the second target station", *Trans. Am. Nucl. Soc.*, **124**, 1, pp. 680–683.

Zavorka, L., et al. (2022), "Optimizing the world's brightest cold-neutron source", *Nucl. Instrum. Methods Phys. Res., Sect. A*, submitted for publication.

2.8. List of abbreviations and acronyms

CHESS	Chopper Spectrometer Examining Small Samples
CAD	computer-aided design
CSG	constructive solid geometry
dpa	displacements per atom
kerma	kinetic energy of radiation produced per unit mass in matter

ORNL	Oak Ridge National Laboratory
PBW	proton beam window
SNS	Spallation Neutron Source
STS	Second Target Station
UM	unstructured mesh

3. Shielding at the European Spallation Source: From Monte Carlo simulations to Reality

Günter Muhrer
European Spallation Source ERIC
Corresponding Author(s): gunter.muhrer@ess.eu

The European Spallation Source is currently being constructed in the Lund, Sweden. As expected for a megawatt class facility, the need for shielding is high, extensive and costly. In support of the project a large number of Monte Carlo particle transport calculations have been performed. As for any simulations, even if one attempts to simulate everything in details, reality will not always play by the roles of the Monte Carlo codes. In this presentation same lessons learned will be given from the experience ESS has gained going through this process.

4. Simulation of Spallation Target Activation and Cask Dose Shieldding

Josef Svoboda, Michael Mocko
Los Alamos National Laboratory
Corresponding Author(s): svoboda@lanl.gov

During the 2022 maintenance outage, we are installing a new generation of spallation target-moderatorreflector-shield (TMRS), known as Mark-IV for Manuel Lujan Jr. Neutron Scattering Center (Lujan Center) at the Los Alamos Neutron Science Center (LANSCE). This paper discusses the activation analysis of the previous target Mark III, in service 2010-2021. The TMRS employs a split target geoometry consisting of two cylindrical W targets positioned on the axis of the proton beam. The upper target has a cylindrical inconel shell filled with seven W discs, with thicknesses increasing downstream. The tungsten discs have Ta cladding and are surrounded by cooling water flowing through the spaces between them. The lower target is a single W-cylinder cladded with Ta surrounded by an inconel shell. These two targets are expected to be the hotspots from an activation perspective,including its cladding and the shell. Another significant activation contribution is expected to be from the proton beam window located above the upper target. The area around the targets is mostly filled with beryllium. However, there is stainless steel (SS) at the bottom of the lower target. Around the proton beam window, there is mainly SS as well. These materials act in part as self-shielding.

However, to ensure radiation safety, Mark III was placed in a steel-lead shielding cask. Activation of designated hotspots was calculated by combining MCNPX 2.7.0 [1] with CINDER 1.05 [2] codes. The final dose simulation was carried out by MCNPX using a gamma dose mesh tally and a set of point detectors (PD). The Mark III target was operated for 12 years with approximately half-year run cycles delivering 800 MeV proton beam. Simulations were compared with the Radiation Control Technician (RCT) measurement on the day Mark-III was taken out and placed into a shielding cask.

[1] Mckinney, Gregg. (2011). MCNPX User's Manual, Version 2.7.0.

[2] S. T. Holloway, W. B. Wilson et al., A Manual for cinder2008 Codes and Data (LA-UR 11-00006),

5. The ORNL R2S Code Suite (ORCS) for Shutdown Dose Rate Simulations

Bor Kos, Kara Godsey
Oakridge National Laboratory
Corresponding Author(s): kosb@ornl.gov

Current experimental fusion systems and conceptual designs of fusion pilot plants (FPPs) are growing in complexity and size. Several radiation metrics are crucial to the safe operation of fusion machines, including the shutdown dose rate (SDDR). SDDR is caused by decay gamma rays from radionuclides that become activated by neutrons during the operation of a fusion system. The two state-of-the-art approaches for determining SDDR are the Direct 1-Step method (D1S) and the Rig orous 2-Step method (R2S).

The R2S method is divided in to 2 steps. In the first neutron transport step, spectra are calculated on a mesh covering the complete problem geometry. The calculated neutron spectra are then used in the intermediate isotope inventory calculation step where the decay gamma spectra and specific activities are calculated. The second transport step follows, where gamma rays originating from the activated radionuclides are transported through the system in question. The high computational demand of the R2S technique originates from the need for two transport simulations in complex and often highly attenuating geometries.

There is a clear need for computationally efficient R2S codes for high fidelity analyses of complex, realistic fusion geometries. The Multi Step Consistent Adjoint Driven Importance Sampling (MSCADIS) variance reduction method was developed with the SDDR problem in mind. The MS-CADIS methodology is implemented in the Oak Ridge National Laboratory R2S Code Suite (ORCS).

In this paper we will present the capabilities of individual codes that make up ORCS. The paper will also include examples of using ORCS to support experimental campaigns at Joint European Torus (JET), analysis of the Pellet Injection system in Port Cell 16 of ITER, and analysis of the Equatorial Port 9 at ITER.

ORCS is under active development with one of the main research areas on integrating the Shift Monte Carlo transport code